Autothermal dry reforming of methane using nickel promoted illite clay catalyst

Mohcin Akri, Tarik Chafik, Pascal Granger, Philippe Ayrault, Catherine Batiot-Dupeyrat

Autothermal dry reforming of methane using novel nickel promoted illite clay catalyst

Mohcin AKRI[1,2], Tarik CHAFIK[2], Pascal GRANGER[3], Philippe AYRAULT[1], Catherine BATIOT-DUPEYRAT[1]*

[1]*Institut de Chimie des Milieux et Matériaux de Poitiers (IC2MP)*

Ecole Nationale Supérieure d'Ingénieurs de Poitiers (ENSIP)

Université de Poitiers - UMR CNRS 7285

1 rue Marcel Doré, TSA 41105, 86073 Poitiers cedex 9 (France)

[2] *Laboratory LGCVR UAE/L01FST, Faculty of Science and Technology of Tangier, University Abdelmalek Essaadi*

[3] *Unité de Catalyse et de Chimie du solide (UCCS)*

Université de Lille 1- UMR CNRS 8181

Cité scientifique Bat C3, 59655 Villeneuve d'Ascq

Abstract

A series of Ni-Ce catalysts supported on illite clays with different amount of cerium were tested with respect to autothermal reforming of methane at 800°C using a GHSV = 60000 $mL.g^{-1}.h^{-1}$. The addition of cerium was found to enhance the catalyst surface area as result of meso-porosity development. Furthermore, the nickel particles size are lowered in the presence of Ce, decreasing the Ni° average size from 34.2 for 10Ni to 16.3nm for 10Ni15Ce. The best catalytic activity and stability were obtained using the catalyst with 15wt% of Ce, which was attributed not only to the redox properties of cerium but also to the better nickel dispersion. On the other hand, the addition of oxygen in the gaseous reactant feed, under the used experimental condition was found to play a key role since the amount of carbon deposition is significantly reduced regardless the catalyst composition.

Keywords: autothermal reforming, illite clay, cerium, nickel

*Corresponding author: catherine.batiot.dupeyrat@univ-poitiers.fr

1. Introduction

Dry reforming of methane to produce syngas is an important process to valorize two major greenhouse contributors. Moreover, the reaction produces syngas with a low H_2/CO ratio suitable for methanol and liquid hydrocarbons from Fischer-Tropsch synthesis [1,2].

Active catalysts are supported noble metals [3-5] and group 8-10 metals such as Fe, Co and Ni [6-8]. Industrially, nickel is the metal of choice due to its inherent availability and low cost compared to noble metals. The major drawback for nickel based catalysts is carbon deposition during the reaction leading to catalyst deactivation. However it has been shown that a high dispersion of the metal species at the surface of the support can limit the coke deposition [1].

Several studies have shown that the nature of the support plays an important role in the catalytic performances. The thermal stability of the support is of particular importance since the reaction has to be conducted at temperatures higher than 750°C. Supports like Al_2O_3, SiO_2, TiO_2, MgO, ZrO_2… exhibited high initial activities but suffered from deactivation [9].

The addition of basic and/or redox promoters can decrease the formation of coke. For example the beneficial effect of alkaline metals such as Mg, Mn, K or Ca was evidenced by Jeong et al. [10]. The authors explain the increase of the catalytic activity by the partial coverage of nickel particles by metal oxide limiting the carbon deposition. Lanthanides were also successfully used to modify the physico-chemical properties of the support. The catalytic stability of the catalyst was enhanced in the presence of La_2O_3 due to the formation of oxycarbonate species which act as dynamic oxygen pool and facilitate coke removal [11,12].

Different studies show that the presence of cerium at the surface of the support promotes the catalytic activity due to the oxygen storage capacity of CeO_2 [13, 14]. Moreover, the decrease of the nickel particles size was observed in the cases of Ce-promoted Ni/Al_2O_3 [15], Ni/SiO_2 [16] and Ni/ZrO_2 [17], while Daza et al. [18] using mesoporous Ni-Ce/clay catalysts showed

that the presence of Ce does not affect the nickel particles size, which was attributed to a strong NiO interaction with the support compared to the NiO-CeO_2 interaction.

Clays are interesting catalytic supports due to their great availability, low cost and specific physico-chemical properties for the dry reforming of methane. Synthetic clays like hydrotalcites promoted with cerium are relatively active and stable at low temperature (550°C) as shown by Debek et al. [19]. At 700°C good catalytic performances and high stability were obtained using a catalyst prepared by doping Ni-Mg-Al mixed oxide with $[Ce(EDTA)]^-$ [20]. The use of natural clays as starting catalytic support was reported, the materials are generally used after modification of their inter-laminar space. The incorporation of alumina species into the inter-laminar spaces of smectite provided a thermal stability to the material avoiding its collapse during the calcination step [21].

Illite is among the abundands phases encountered in natural clays mineral contained in sedimentary rocks. The formation of illite results from the transformation of smectite during diagenesis and metamorphism [22]. Illite is known as interlayer-deficient dioctahedral minerals of the mica group with general formula: $(K,Ca,Mg)(Al,Mg,Fe)_2(Si,Al)_4O_{10}[(OH)_2,(H_2O)]$ [23]. Illite has commonly K in its interlayer site which gives an overall basal spacing of 1.0 nm [24]. Up to now, illite containing clays were used as low-cost adsorbents for industrial waste treatment [25].

The aim of the present study was to study the performances of illite-based catalysts with respect to the dry reforming of methane, which to the best of our knowledge has never been reported before. The catalysts were prepared using a simple impregnation method of nitrate precursors. The influence of cerium addition to the support was investigated, while the amount of nickel was fixed at 10% in weight. Moreover this paper highlights the interest of coupling carbon dioxide reforming with partial oxidation of methane to syngas following the

operating conditions optimized according to thermodynamic analysis carried out by N. Amin and T.C. Yaw [26].

2. Experimental

2.1 Catalysts preparation

The starting material is a natural morocco clay from the area of Tanger. Illite was separated from the raw clay by wet sedimentation according to the Stokes law. This technic allowed to remove the more dense particles such as quartz. The raw clay is dispersed in deionized water (10% in weight) and submitted to vigorous stirring during four hours until a complete homogenization of the suspension was obtained. The suspension is left for decantation during 24 hours, the recovered suspension is dried at 100°C during 24 hours and then calcined at 500°C during 4 hours before the impregnation step.

The catalytic species were deposited on the clay surface using co-impregnation method by adding the corresponding amount of nitrate precursor for nickel and cerium. The resulting materials were dried at 120°C during 24 hours and then calcined at 500°c during 4 hours.

2.2 Catalysts characterization

The composition of catalysts was determined by Atomic Emission Spectroscopy with Induced Coupled Plasma (ICP-AES/Optima 200 DV, Perkin Elmer instrument).

The catalysts were characterized by powder X-ray diffraction using a BRUKER AXS D5005 diffractometer with $CuK_{\alpha 1}$ = 1,5406 and $CuK_{\alpha 2}$ =1.5439 Å, operated at 40kV and 40mA. The diffraction patterns were recorded in the 2θ values range 3-80° with a step size of 0.01° and 1s per step. Phase identification was performed by comparison with the information of the JCPDS database.

Transmission electron microscopy (TEM) was carried out on a JEOL 2100 electron microscope operating at 200kV, with a LaB_6 filament and equipped with a Gatan ultra scan camera. Microanalysis of Ni, Fe and Ce was carried out by energy dispersive X-ray spectroscopy (EDX) in the nanoprobe mode. The mean particle diameter was calculated from: $d= \sum n_i d_i^3 / \sum n_i d_i^2$. At least 10 photographs were examined while more than 300 particles were measured and the results were normalized to 100%.

TPR experiments were carried out in a Micromeritics Autochem 2910 equipment using about 160 mg of catalyst. A 5% H_2/Ar flow of 50mL.min^{-1} was passed over the catalyst while the temperature was raised at 5°C/min from ambient to 700°C and maintained at this temperature for 2 hours. The amount of hydrogen consumed was measured with a thermal conductivity detector.

Surface areas were measured by the BET procedure; all samples were out gassed for 30 minutes at 623K before analysis. The adsorption – desorption isotherms of N_2 were determined using 30% N_2/He as the adsorbate on a Micromeritics Flowsorb II 2300 apparatus at –196°C.

2.3 Catalytic experiments

The catalysts performances were evaluated at atmospheric pressure, in a fixed bed continuous flow quartz reactor (i.d. = 10 mm) containing 100mg of catalyst sample (see Figure 1). The flow rate of the reactant mixture was 100 mL/min (CH_4/CO_2= 50/50 mL/min or $CH_4/CO_2/O_2$= 50/40/10 mL/min; GHSV=6.0×10^4 mL.g^{-1}.h^{-1}). The temperature was increased from room temperature to 800 °C at a rate of 5 °C/min, and kept during the desired reaction time. The temperature was measured with a thermocouple located inside the reactor but without direct contact with the catalyst. The reaction products were analyzed by a micro-GC.

3 Results and discussions

3.1 Characterization of the clay support and the catalysts

The chemical composition of the pretreated illite material is reported in Table 1. As expected the clay contains mainly SiO_2 and Al_2O_3 but also a significant amount of iron oxide. A similar composition was reported by Gailhanou et al. for a typical illite containing clay [27]. The designation of materials, reported in Table 2, is based on the theoretical amount of nickel and/or cerium (in weight percent) highlighting the targeted values and those obtained with elemental analysis.

The XRD pattern of the clay material calcined at 500°C (Figure 2 (a)) exhibits the typical reflections of illite with an interlayer space d_{001} = 1 nm at 2θ= 8.8° [28] The presence of quartz can also be seen (JCPDS n° 5-490).

After addition of nickel on the illite clay, broad peaks of NiO are observed (JCPDS n° 01-078-0423, Figure 2 (b)). For cerium loaded catalysts, broad peaks attributed to the fluorite-type structure of CeO_2 are visible, the relative intensities of CeO_2 signal increasing with the amount of cerium content [29].

The surface area value for illite calcined at 500°C, obtained by applying the BET method, is 19 $m^2.g^{-1}$. The addition of cerium leads to the generation of porosity as shown in Table 3. The isotherms are different for the non-promoted and Ce-promoted illite (Figure 3). Thus the isotherms seem to be likely of type-I for illite clay, while the hysteresis loop of type IV isotherm is shown for Ce-based catalyst. The BJH pore size distribution indicates the formation of pores in the mesoporous region with an average size of 15.2 nm.

The H_2-TPR profiles (Figure 4) show three main regions of reduction, two corresponding to the illite support and the first region, at the lowest temperature, corresponding to the reduction of NiO into metallic nickel. The only reducible species in illite is Fe_2O_3 present in the

octahedral sites of the clay. The reduction proceeds, apparently, following two steps according to equations (1) and (2) [30]:

$3Fe_2O_3 + 3H_2 = 6FeO + 3\ H_2O$ (1)

$FeO + H_2 = Fe + H_2O$ (2)

The peak corresponding to NiO reduction is shifted to lower temperature when the Ce content is increased. The promoting effect of Ce species for NiO reduction can be attributed to the existence of Ce^{3+}/Ce^{4+} redox pairs, which enable the electron transfer favoring the reduction of NiO species in the neighbouring sites [19, 20].

The hydrogen consumption was determined by decomposition of the peaks using the mathematical software Origin as shown in Figure 5. Hence, table 4 summarized the amount of hydrogen consumed determined by TPR and the hydrogen volume required to reduce NiO, obtained based on the elemental composition. Note that the reducibility of nickel oxide is not affected by the amount of cerium content since it is closed to 100% within the experimental error (estimated at ± 2% of the indicated value).

According to the H_2-TPR profiles, it was decided to perform the reduction of the starting material at 600°C under hydrogen prior to the reaction, in order to obtain the active metallic nickel particles.

The XRD patterns obtained after the reduction step reported in Figure 6 shows mainly the presence of reduced Ni° as revealed by reflections at 2θ= 44.5 and 54°. Nevertheless, the sizes of Ni particles were not possible to determine from XRD due to the low intensity of the resulting signal. Thus Transmission Electron Microscopy was used to determine the average size of Ni as indicated below. No significant modifications of the illite support was observed by XRD. Note that the surface area of the catalysts after the reduction step (Table 3) decreases significantly showing the negative effect of the reduction step regardless the Cerium content.

TEM analysis performed after the reduction step clearly show the presence of spherical particles of nickel (Figure 7) whereas EDX analysis reveals the presence of small size Ni-Fe alloy particularly in the case of 10%Ni/illite while it is not detected for the 10%Ni-15%Ce/illite material. Consequently, it is suggested that the presence of cerium at the surface of illite prevents the reaction between iron and nickel avoiding the formation of the alloy which is not active in the reaction of methane dry reforming [31].

The nickel particle size distribution was evaluated using TEM analysis after the reduction step for both the 10%Ni/illite and 15% Ce containing:10Ni15Ce catalysts (Figure 8). It was found for 10%Ni/illite, that nickel particles diameter ranges between 5 and 100 nm with an average diameter of 34.2 nm. In the presence of cerium smallest nickel particles are evidenced as indicated by average size around 16.3 nm. Hence, the addition of cerium leads to a better nickel dispersion on the support as also reported by Li et al. [16] for Ce-promoted Ni/SiO_2 catalysts.

3.2 Catalytic activity

The catalytic experiments were carried out using a mixture of methane and carbon dioxide without inert gas diluent. The reaction was performed at 800°C, using low contact time in order to avoid thermodynamic limitations (Gas Hourly Space Velocity = 60000 $mL.h^{-1}.g^{-1}$).

3.2.1 Influence of the presence of oxygen in the gas feed

Thermodynamic equilibrium was calculated using the software HSC chemistry 5. The results obtained without oxygen and with 10% vol. O_2 in the feed are gathered in Figure 9. The optimal amount of oxygen in the feed gases was chosen according to operating conditions reported by Amin and Yaw corresponding to $CH_4/CO_2/O_2$ ratio of 1/0.8/0.2 at temperatures higher than 1000K [26]. Experiments carried out with the 10Ni15Ce catalyst, using a

stoichiometric mixture of methane and carbon dioxide without oxygen, show an initial methane conversion of 72% that decreases to 55% after four hours of reaction. The same trend is observed for carbon dioxide conversion, showing a catalyst deactivation during time on stream most probably due to carbon deposition. The addition of oxygen into the feed strongly increases the methane conversion, while CO_2 conversion remains unaffected since complete oxidation of CH_4 into CO_2 probably occurs. Moreover the addition of oxygen into the feed allows to maintain methane conversion at high level ranging from 88 to 84% after reaction. The H_2/CO molar ratio was comprised between 0.78 and 0.65 without oxygen due to the occurrence of the Reverse Water Gas Shift reaction (RWGS). Note that in the presence of oxygen the latter reaction is likely not occuring and the H_2/CO molar ratio is closed to unity. So far, the combined partial oxidation and dry reforming of methane on clay support was reported only by Liu et al. using vermiculite as catalyst support [32]. The authors reported similar results with respect to CH_4 and CO_2 conversions, but higher contact time was used and no comparison was made with experiments performed in the absence of oxygen into the feed.

3.2.2 Influence of the amount of Ce in Ni-Ce-promoted illite clay

Figure 10 shows that in the absence of cerium, CH_4 and CO_2 conversions sharply decrease with time on stream. Whereas the presence of CeO_2 on clay support increases significantly the catalytic activity and limit the catalytic deactivation. Note that we obtained the best catalytic performances with 10Ni15Ce, an increase of the Ce amount until 20% wt. is not favorable most probably due to embeddement of nickel particles into cerium oxide making them not accessible for the reactant adsorption. After four hours of reaction, a decrease of the surface area is observed whatever the amount of cerium used (Table 2). However the catalytic activity is not significantly affected by this textural modification since methane conversion is only decreased from 88 to 84% with 10Ni15Ce.

The beneficial effect of cerium was already shown by Osawa et al. [33] using alumina as support. The Ce-promotion effect was also evidenced using delaminated-type smectite support [18]. The authors reported that the presence of cerium does not modify the dispersion of metallic nickel particles probably due to the relative high surface area of the materials ($80 m^2/g$) compared to the illite based catalyst we used ($\approx 20 m^2/g$). The better catalytic activity of the Ce-promoted catalyst was attributed to the presence of oxygen vacancies in fluorite structure facilitating CO_2 adsorption and gasification of the CH_x species according to equations (3) and (4) [34]:

$$Ce_2O_3 + CO_2 \rightarrow 2CeO_2 + CO \quad (3)$$

$$4CeO_2 + C \rightarrow 2\ Ce_2O_3 + CO_2 \quad (4)$$

Over the Ce-promoted illite support, nickel particles are well dispersed at the surface as revealed by TEM analysis. The higher Ni dispersion in the case of Ce containing catalyst as compared to Ni/illite seems to, not only, limit coke formation but increases also the activity and stability of the catalyst [35]. This is evidenced by thermogravimetric analysis carried out after four hours of catalyst operating in order to determine the coke deposition. As shown in Figure 11, the weight gain observed corresponds to the oxidation of the metallic active sites, whereas the weight loss, between 525 and 675°C, is very low for 10Ni15Ce but also for 10Ni, it is closed to only 2% for the two catalysts. Although, the low amount of carbon deposition observed on the catalyst 10Ni can be attributed to its low catalytic activity as well as the presence of oxygen in the gas feed which avoid the carbon deposition according to:

$$C + ½\ O_2 \rightarrow CO \quad (5)$$

In the presence of cerium, it is possible to suggest that oxygen plays also a key role for the re-oxidation of Ce_2O_3 into CeO_2. The surface defects of ceria may provide sites for oxygen adsorption and restoring Ce^{4+} sites [36,37]. Consequently, under the used experimental conditions, in addition to reforming and partial oxidation of methane: equations (3) and (4), a

third reaction (equation 6) might be taken into account in order to explain the prevention of coke deposition:

$$Ce_2O_3 + 1/2\ O_2 \rightarrow 2\ CeO_2 \qquad (6)$$

Conclusions

The illite containing natural clay seems to be a supportof interest for the reaction of autothermal reforming of methane at 800°C for a series of Nickel –cerium catalysts. The addition of cerium was found to increase significantly the specific surface area of the catalyst and the dispersion of nickel particles at the surface of the illite support. The best catalytic activity and stability were obtained with the catalyst containing 15% in weight of Ce. Moreover, the use of oxygen in gas feed with a $CH_4/CO_2/O_2$ ratio of 1/0.8/0.2 allows to maintain high methane and carbon dioxide conversions during four hours of reaction. Under these condition, the carbon deposition remains significantly low, proving that oxygen plays a key role in the reaction mechanism involving, most probably, in the redox Ce^{3+}/Ce^{4+} cycle.

Acknowledgements

The authors greatly acknowledge the financial support from Volubilis (MA/13/288- Campus France N°29091UK) and the Erasmus Mundus - Al Idrisi II program

References

[1] J.R. Rostrup-Nielsen, J. Sehested, J.K. Norskov, Adv. Catal. 47 (2002) 65-139

[2] S.C. Tsang, J.B. Claridge, M.L.H. Green, Catal. Today, 23 (1995) 3-15

[3] J.T. Richardson, S.A. Paripatyadar, Appl. Catal. 61 (1990) 293-309

[4] A.T. Ashcroft, A.K. Cheetman, M.L.H. Green, P.D.F. Vernon, Nature 352 (1991) 225

[5] F. Solymosi, G. Kutsan, A. Erdöhelyi, Catal. Lett. 11 (1991) 149-156

[6] O. Yamazaki, T. Nozaki, K. Omata, K. Fujimoto, Chem. Let. (1992) 1953-1954

[7] Y.H. Hu, E. Ruckenstein, Catal. Lett. 36 (1996) 145-149

[8] U. Slagtern, R.Olsbye, I. M. Blom, H. Dahl, Fjellvag, Appl. Catal. A 145 (1996) 375-388

[9] M. Usman, W.M.A. Wan Daud, H. F. Abbas, Renew Sustain. Energy Rev. 45 (2015) 710-744

[10] H. Jeong, K. Kim, D. Kim, I. Song, J. Mol. Cat. 246 (2006) 43-48

[11] J.Z. Luo, Z.L. Yu, C.F. Ng, C.T. Au, J. Catal. 194 (2000) 198-210

[12] A. Serrano-Lotina, A.J. Martin, M.A. Folgado, L. Daza, Int. J. Hydrogen Energy 37 (2012) 12342-12350

[13] R. Craciun, B. Shereck, R.J. Gorte, Catal. Lett. 51 (1998) 149-153

[14] H.C. Yao, Y.F.Y. Yao, J. Catal. 86 (1984) 254-265

[15] W. Chen, GF. Zhao, Q.S. Xue, L. Chen, Y. Lu, Appl. Catal. B : Env. 136 (2013) 260-268

[16] B. Li, X. Xu, S. Zhang, Int. J. Hydrogen Energy 38 (2013) 890-900

[17] A. Pietraszek, B. Koubaissy, A.C. Roger, A. Kiennemann, Catal. Today 176 (2011) 267-271

[18] C. E. Daza, O.A. Gamba, Y. Hernandez, M. A. Centeno, F. Mondragon, S. Moreno, R. Molina, Catal. Lett 141(2011) 1037-1046

[19] R. Debek, M. Radlik, M. Motak, M. E. Galvez, W. Turek, P. Da Costa, T. Grzybek, Catal. Today, in press 2015 doi 0920-5861

[20] C. E. Daza, J. Gallego, F. Mondragon, S. Moreno, R. Molina, Fuel 89 (2010) 592-603

[21] C. E. Daza, A. Kiennemann, S. Moreno, R. Molina, Appl. Catal. A: gen. 364 (2009) 65-74

[22] T. Kimura, H. Kawashima, I. Saito, Int. J. Coal Geol. 26 (1994) 215-231

[23] A. Cremers, A. Elsen, P. Depreter, A. Maes, Nature, 335 (1988) 247-249

[24] A. J. Fuller, S. Shaw, M. B. Wrd, S.J. Haigh, J. Frederick, W. Mosselmans, C. L. Peacock, S. Stackhouse, A.J. dent, D. Trivedi, I.T. Burke, Appl. Clay Science 108 (2015) 128-134

[25] K.R. Ramakrishna, T. Viaraghavan, Water Sci. technol. 36 (1997) 189-196

[26] N. A. S. Amin, T.C. Yaw, Int. J. Hydrogen Energy, 32 (2007) 1789-1798

[27] H. Gailhanou, P. Blanc, J. Rogez, G. Mikaelian, H. Kawaji, J. Olives, M. Amouric, R. Denoyel, S. Bourrelly, V. Montouillout, P. Vieillard, C.I. Fialips, N. Michau, E.C. Gaucher, Geochim. Cosmochim. Acta 89 (2012) 279-301

[28] H.M. Baioumy, M.H.M. Gharaie, Appl. Clay Sci. 42 (2008) 318–325

[29] D.K. Kim, K. Stöwe, F. Müller, W.F. Maier, J. Catal. 247 (2007) 101-111

[30] J. Zielinski, I. Zglinicka, L. Znak, Z. Kaszkur, Appl. Catal. A: Gen. 381 (2010) 191-196

[31] H. Provendier, C. Petit, C. Estournes, A. Kiennemann, Stud. in Surf. Sci. Catal. 119 (1998) 741-746

[32] Y. Liu, Z. He, L. Zhou, Z. Hou, W. Eli, Catal. Comm. 42 (2013) 40-44

[33] T. Osawa, Y. Nakai, A. Mouri, I.Y. Sandy Lee, Appl. Catal. A: Gen. 474 (2014) 100-106

[34] S.M. Lima, J.M. Assaf, M.A. Pena, J.L.G. Fierro, Appl. Catal. A: Gen 311 (2006) 94-104

[35] G. Sierra, J. Gallego, C. Batiot-Dupeyrat, J. Barrault, F. Mondragon, Appl. Catal. A: Gen 369 (2009) 97-103

[36] Y. Wu, T. Yu, B.S. Dou, C.X. Wang, X.F. Xie, Z.L. Yu, S.R. Fan, Z.R. Fan, L. C. Wang, J. Catal. 120 (1989) 88-107

[37] L. Pino, A. Vita, M. Lagana, V. Recupero, Appl. Catal. B: Env. 148-149 (2014) 91-105

Tables captions

Table 1: Chemical composition of the illite clay (wt. %)

Table 2: Designation and elementary composition of catalysts

Table 3: BET surface area of illite and Ni-Ce/illite (m^2/g)

Table 4: Hydrogen consumption by H_2-TPR

Figures captions

Figure 1: Experimental setup

Figure 2: XRD patterns of the materials after calcination at 500°C a) illite, b) 10Ni, c) 10Ni5Ce, d) 10Ni10Ce, e) 10Ni15Ce, f) 10Ni20Ce
× Illite, Q quartz, ◊ CeO_2, Δ NiO, S alloy Fe-Cr-Al

Figure 3: N_2 adsorption-desorption isotherms and pore size distribution obtained from the adsorption loop for illite and 10Ni15Ce

Figure 4: H_2-TPR profiles of illite materials

Figure 5: H_2-TPR profile for 10Ni10Ce with peak decomposition using Origin software

Figure 6: XRD patterns of the materials after reduction at 600°C under hydrogen
× Illite, Q quartz, ◊ CeO_2, ∗ Ni°, S alloy Fe-Cr-Al

Figure 7: TEM and EDX analysis of 10Ni

Figure 8: TEM analysis and particle size distribution after reduction of 10Ni and 10Ni15Ce

Figure 9: CH_4, CO_2 conversions, H_2/CO ratio over 10Ni15Ce, T= 800°C, CH_4/CO_2 = 50/50 and $CH_4/CO_2/O_2$ = 50/40/10, GHSV = 60000 $mL.h^{-1}.g^{-1}$

Figure 10: CH_4, CO_2 conversions, H_2/CO ratio over Ni-based illite clays with different amount of Ce

Figure 11: TGA oxidation curves after 4 hours of reaction on 10Ni and 10Ni15Ce catalysts, T= 800°C, $CH_4/CO_2/O_2$ = 1/0.8/0.1, GHSV = 60000$mL.h^{-1}.g^{-1}$

Table 1:

SiO_2	Al_2O_3	MgO	Fe_2O_3	K_2O	CaO	TiO_2
54.4	26.6	2.1	7.6	5.8	0.4	1.4

Table 2:

designation	Ni (wt.%)		Ce (wt.%)	
	T*	M **	T*	M**
10Ni	10	10.2	0	-
10Ni5Ce	10	9.5	5	4.3
10Ni10Ce	10	10.1	10	10.0
10Ni15Ce	10	10.2	15	13.4
10Ni20Ce	10	10.0	20	18.5

*T: Target value
**M: measured value

Table 3:

Sample	Surface area (m^2/g)			Vp (cm^3/g)
	Calc.[a]	Red.[b]	Reac.[c]	
Illite	19	-	-	0.021
15Ce	22	-	-	0.040
10Ni	19	9	5	0.036
10Ni5Ce	19	12	5	0.028
10Ni10Ce	23	14	4	0.054
10Ni15Ce	25	15	6	0.064
10Ni20Ce	26	13	6	0.074

[a] calcined at 500°C

[b] after reduction at 600°C under H_2

[c] after 4 hours of reaction

Table 4:

Catalyst	H_2 consumption for NiO reduction (mL STP/g) (± 2%)		NiO Reductibility (%)
	Estimated*	Determined**	
10Ni	39.1	37.2	95
10Ni5Ce	35.9	36.1	100
10Ni10Ce	38.4	37.3	97
10Ni15Ce	39.0	39.5	100
10Ni20Ce	38.3	38.4	100

*Estimated: calculated from the nominal composition of the material according to the following reaction: $NiO + H_2 = Ni + H_2O$

**Determined: obtained from H_2-TPR by decomposition of the peaks using the mathematical software Origin

Figure 1: Experimental setup

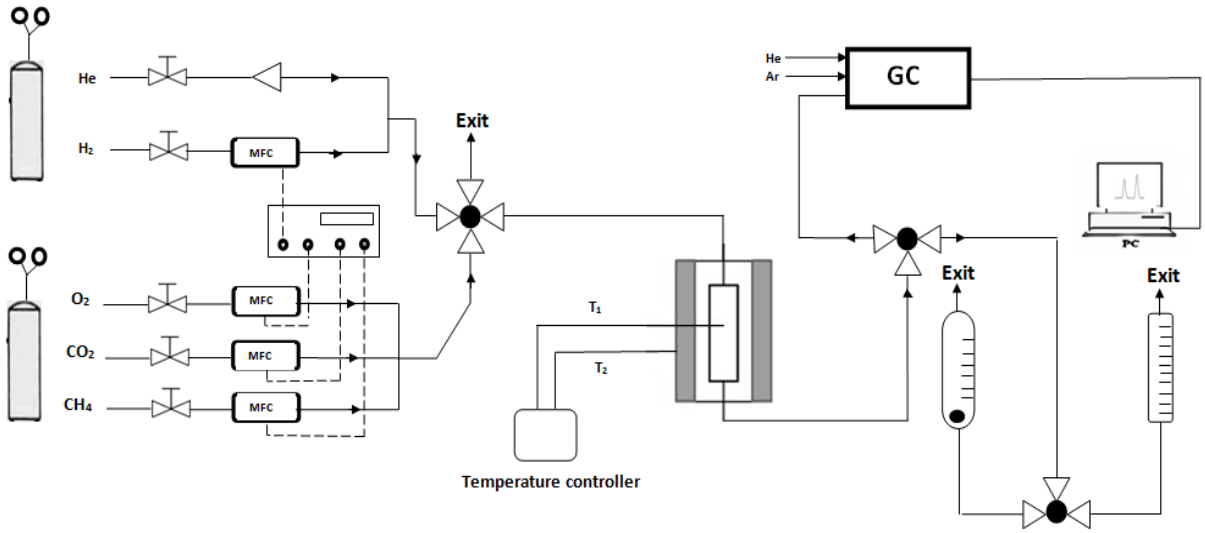

Figure 2:

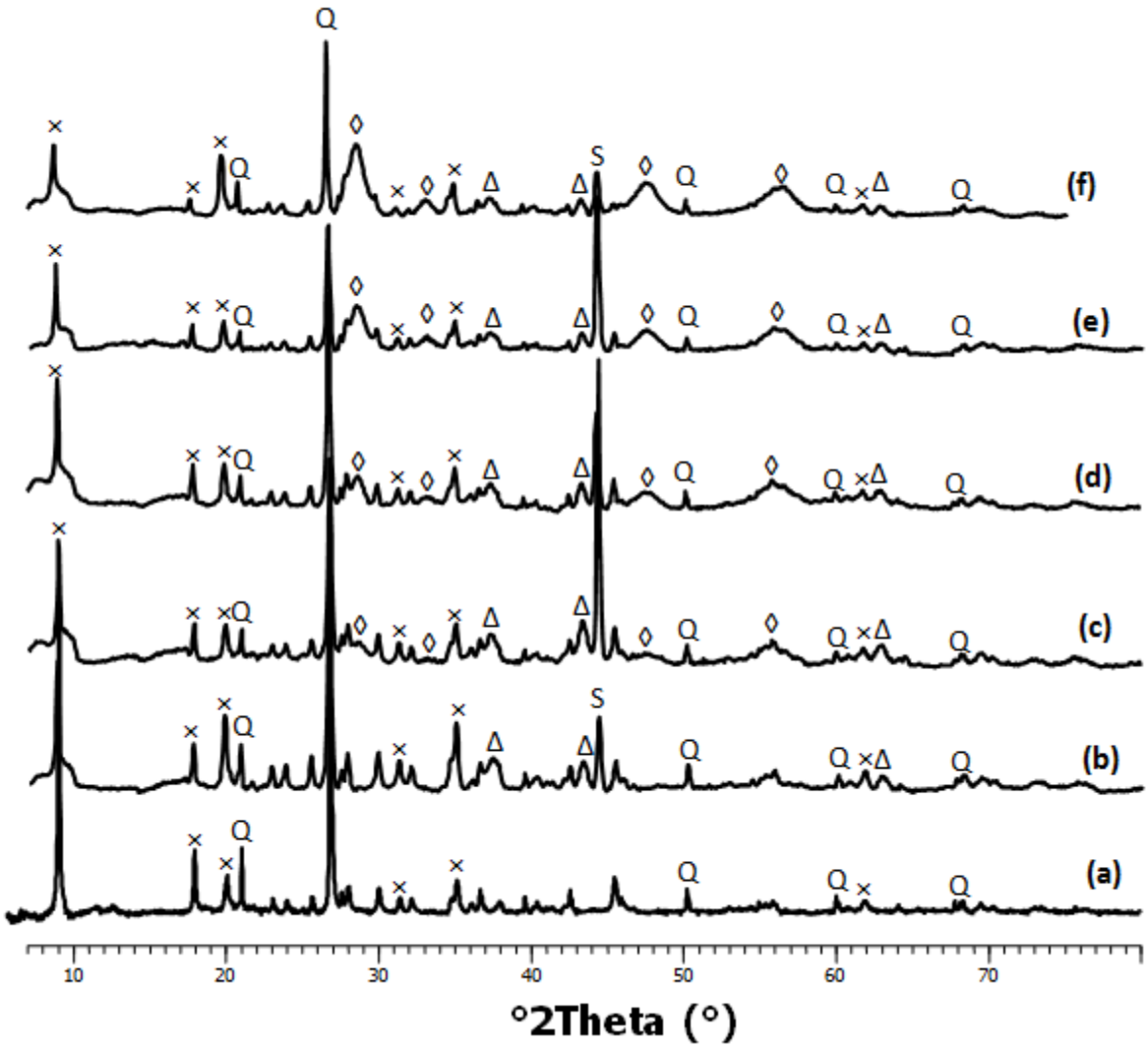

Figure 3

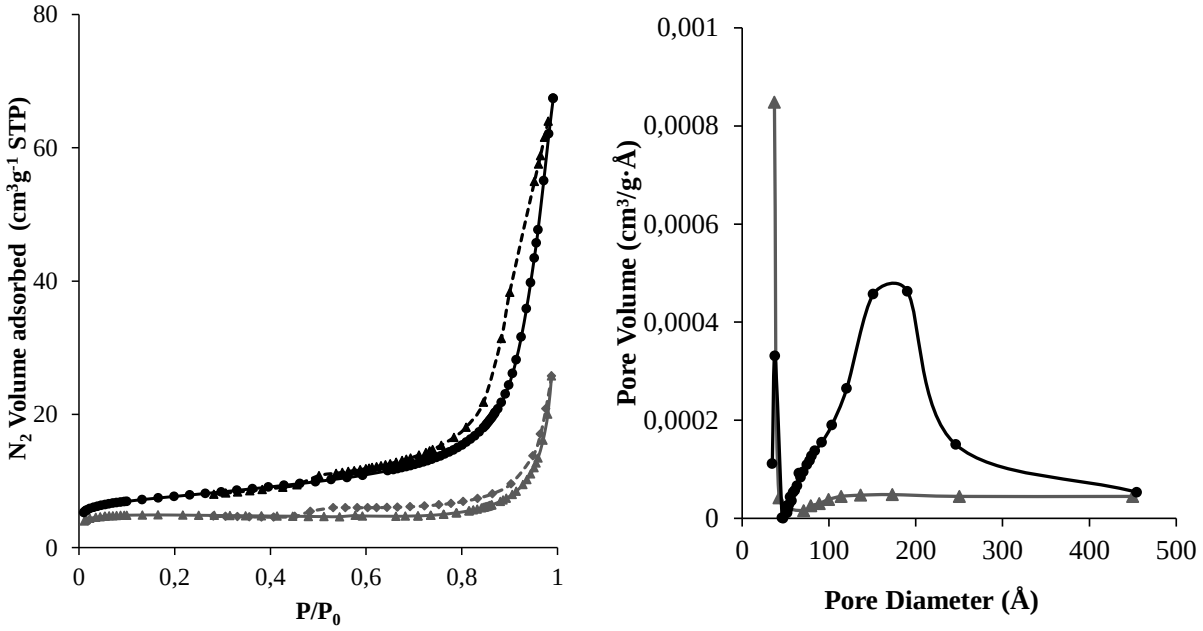
80
60
40
20
0
0
0,2
0,4
0,6
0,8
1
N2 Volume adsorbed (cm3g-1 STP)
P/P0
0,001
0,0008
0,0006
0,0004
0,0002
0
0
100
200
300
400
500
Pore Volume (cm3/g·Å)
Pore Diameter (Å)

Figure 4

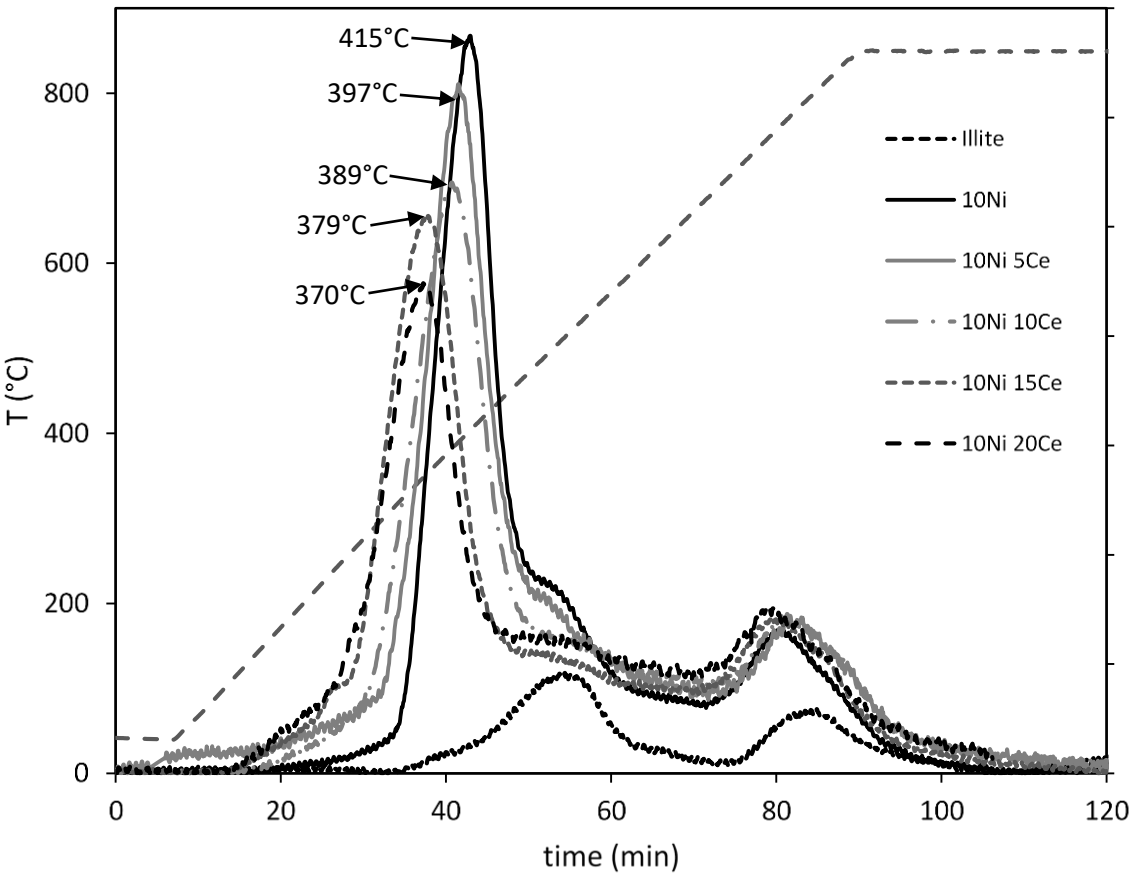
415°C
397°C
389°C
379°C
370°C
Illite
10Ni
10Ni 5Ce
10Ni 10Ce
10Ni 15Ce
10Ni 20Ce
T (°C)
time (min)
0
200
400
600
800
0
20
40
60
80
100
120

Figure 5

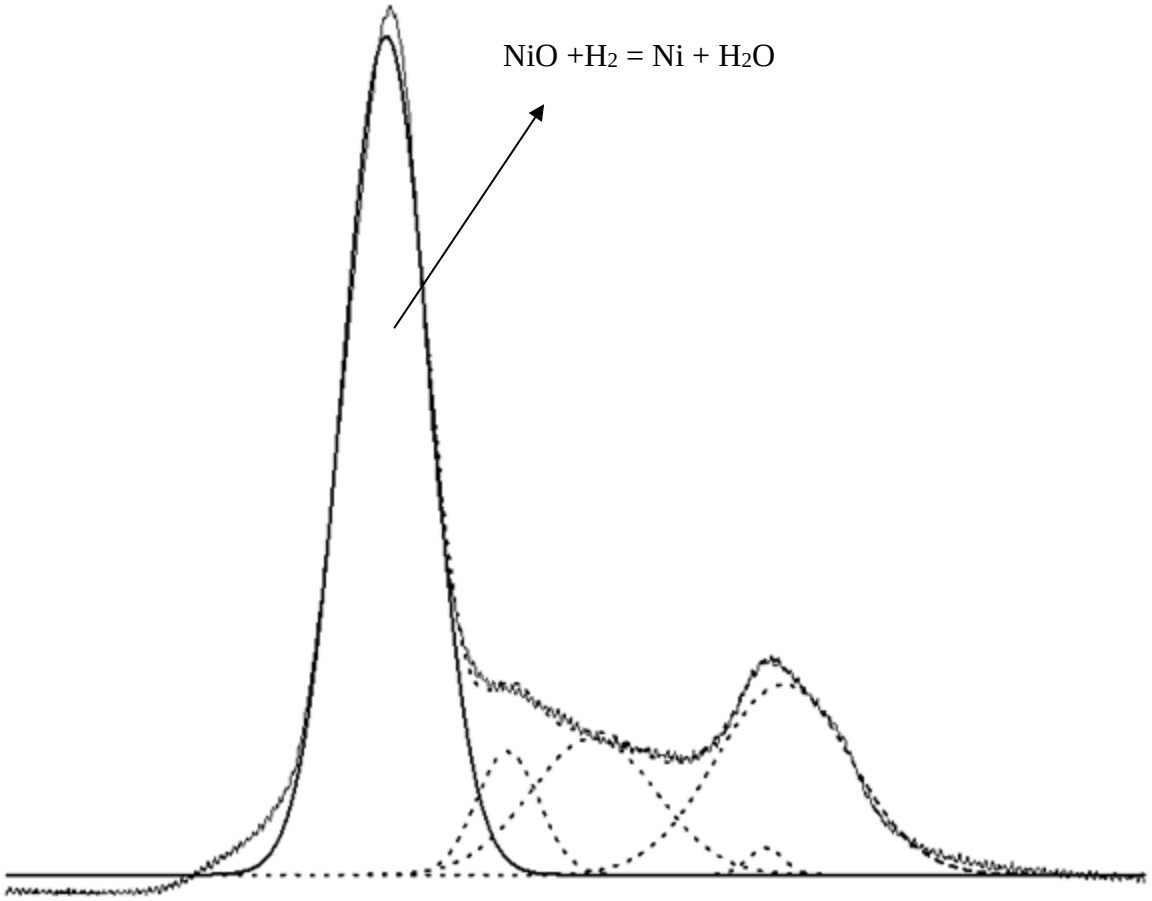

Figure 6: XRD patterns after reduction

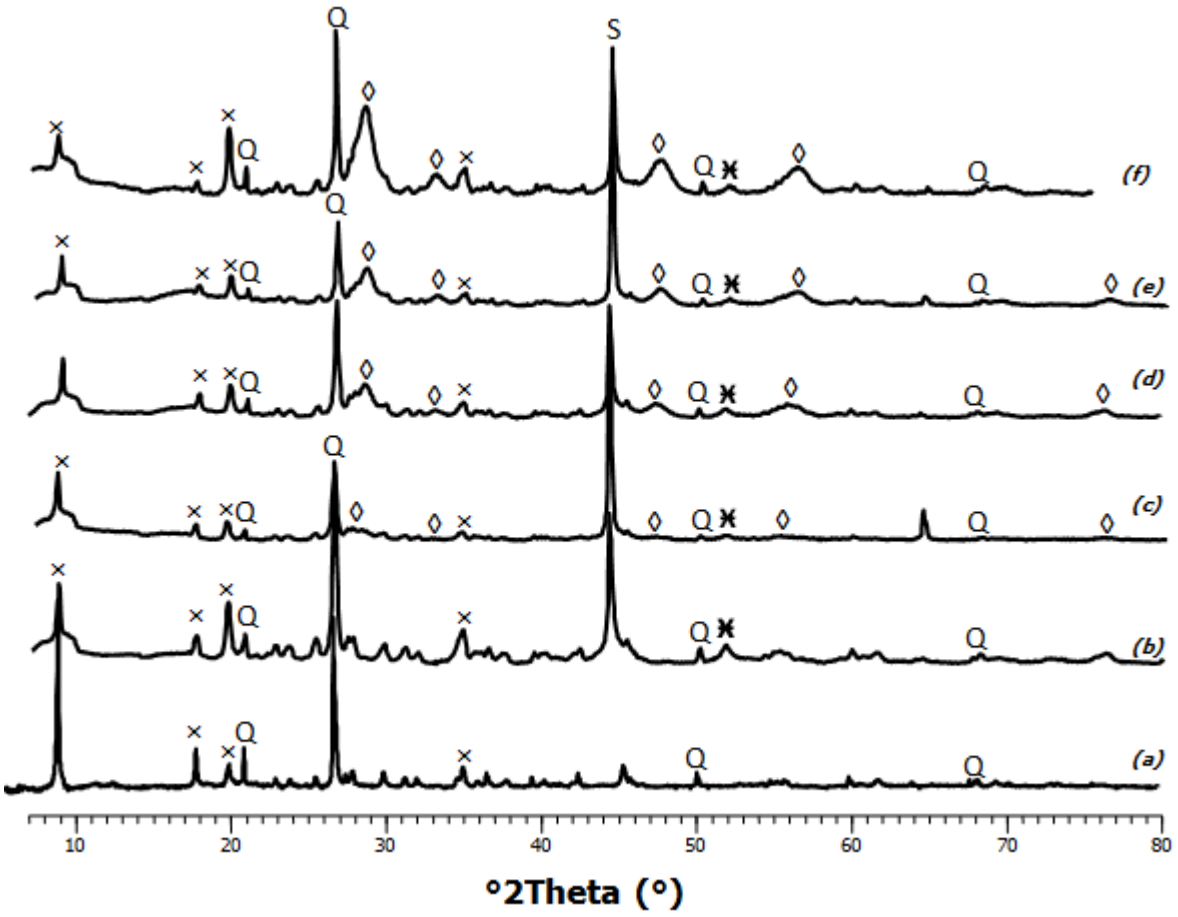

Figure 7:

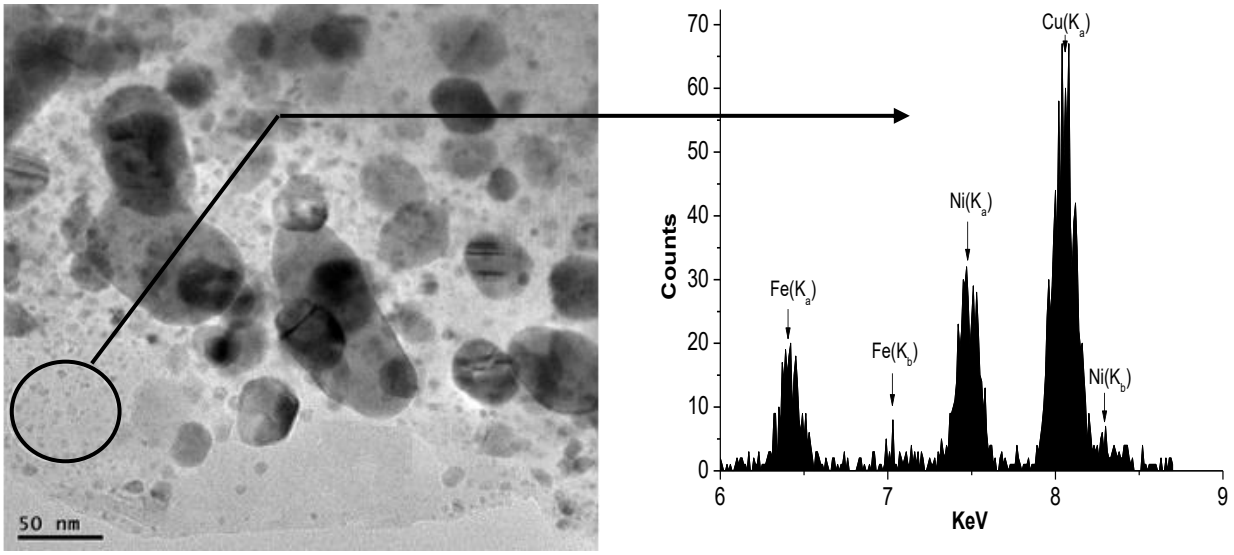
50 nm
Counts
KeV
Fe(K$_a$)
Fe(K$_b$)
Ni(K$_a$)
Cu(K$_a$)
Ni(K$_b$)
0
10
20
30
40
50
60
70
6
7
8
9

Figure 8

a) 10Ni15Ce b) 10Ni

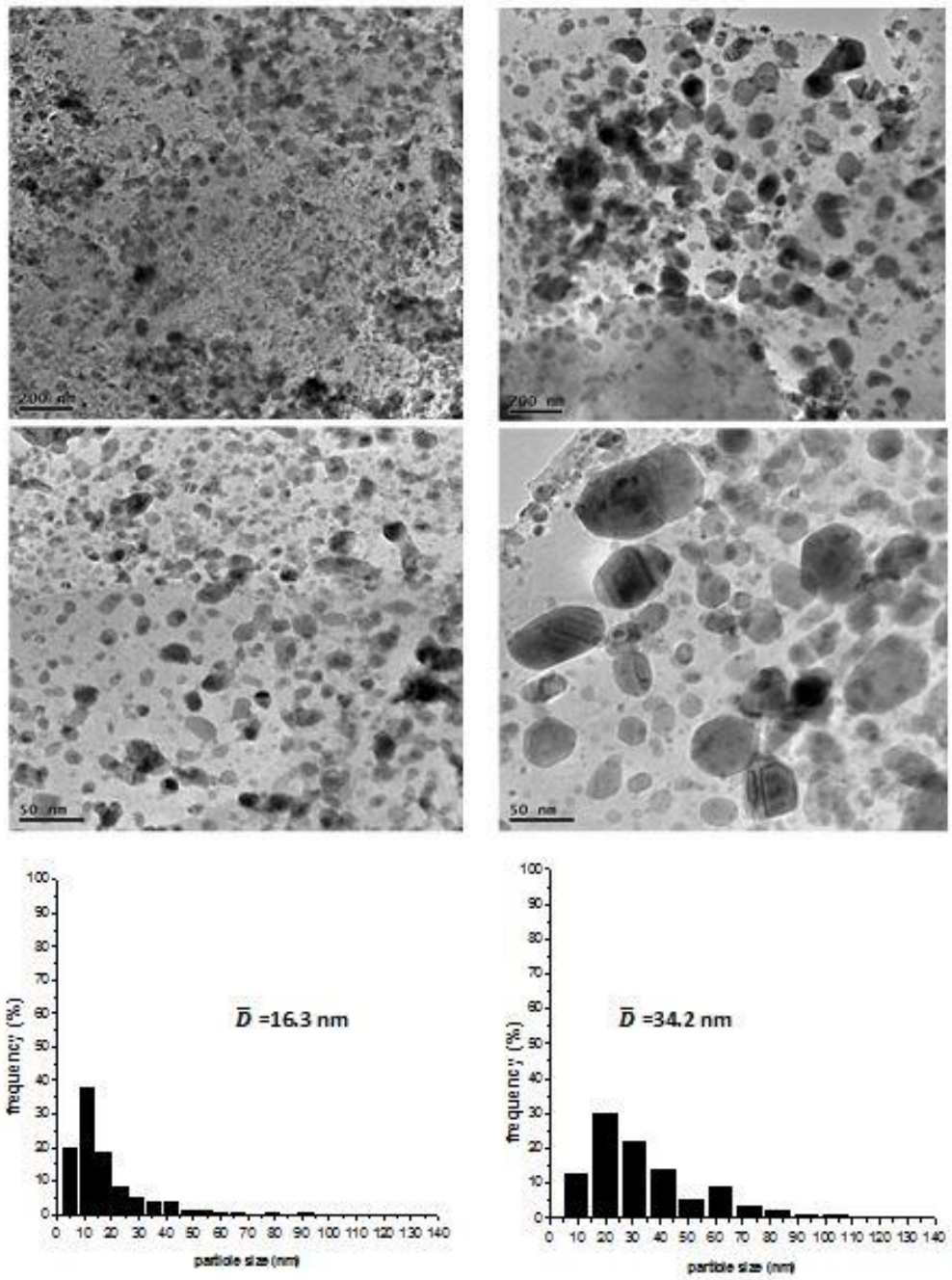

Figure 9:

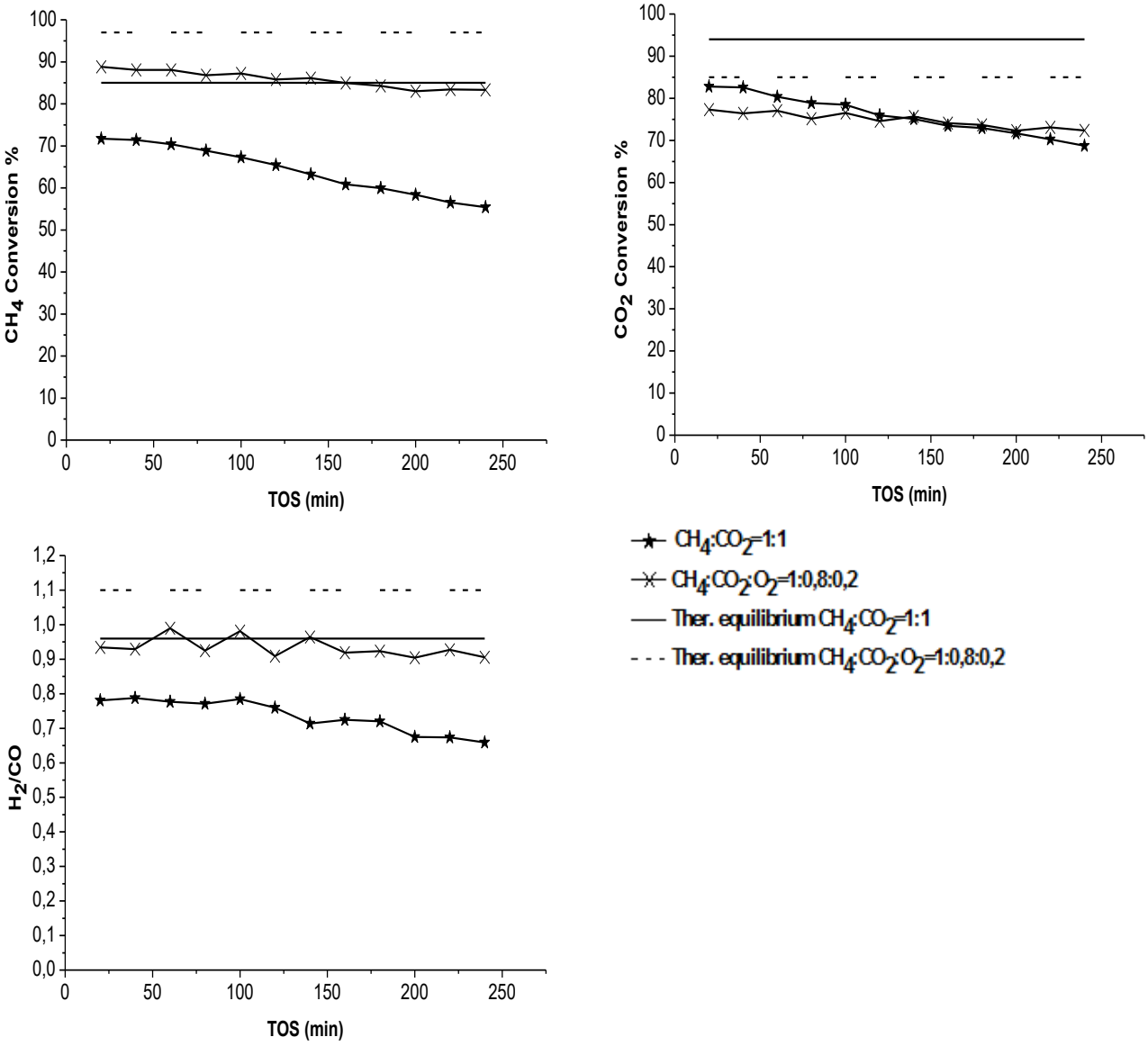
CH4 Conversion %
TOS (min)
CO2 Conversion %
TOS (min)
H2/CO
TOS (min)
CH4:CO2=1:1
CH4:CO2:O2=1:0,8:0,2
Ther. equilibrium CH4:CO2=1:1
Ther. equilibrium CH4:CO2:O2=1:0,8:0,2

Figure 10:

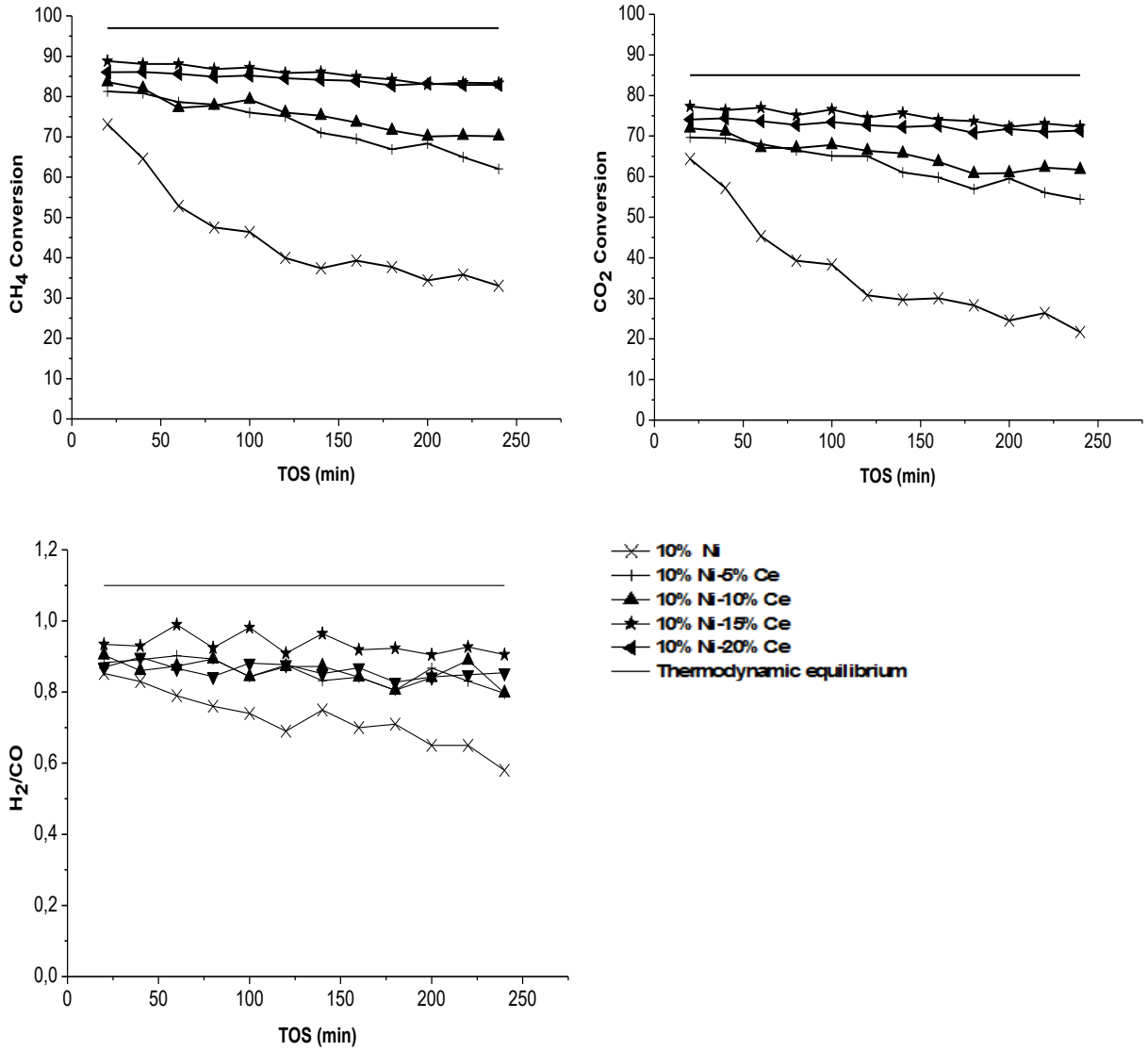
CH4 Conversion
TOS (min)
CO2 Conversion
TOS (min)
H2/CO
TOS (min)
10% Ni
10% Ni-5% Ce
10% Ni-10% Ce
10% Ni-15% Ce
10% Ni-20% Ce
Thermodynamic equilibrium

Figure 11

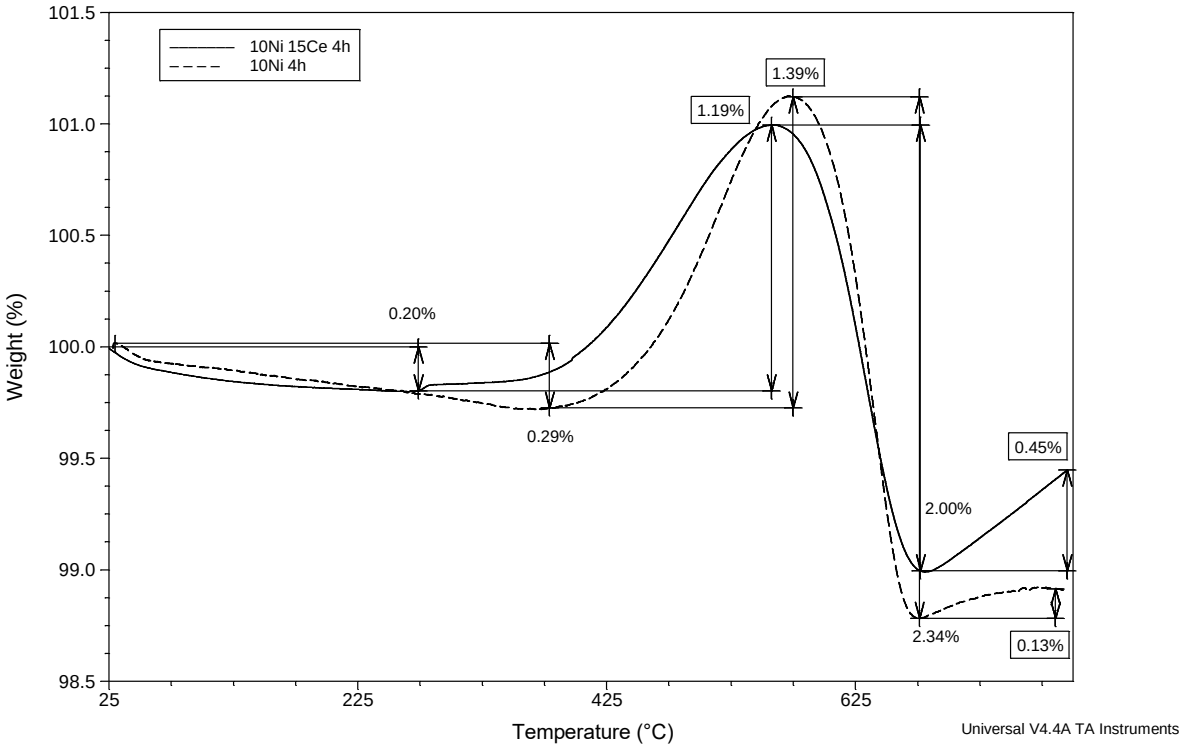
10Ni 15Ce 4h
10Ni 4h
1.39%
1.19%
0.20%
0.29%
2.00%
0.45%
2.34%
0.13%
Weight (%)
Temperature (°C)
101.5
101.0
100.5
100.0
99.5
99.0
98.5
25
225
425
625
Universal V4.4A TA Instruments